JOURNAL OF MATERIALS SCIENCE 31 (1996) 1087–1099

Solid-solution hardening and softening in binary iron alloys

K. OKAZAKI
Department of Materials Science and Engineering, University of Kentucky, Lexington, KY 40506-0046, USA

Six dilute (0.2, 0.5 and 1 at%) binary iron-base alloys with Co, Cr, Al, Si, Mn and Ni were prepared after scavenging inherent carbon with Ti. From tensile and stress relaxation tests in the temperature range of 77 to 450 K, stress–strain behaviours and thermal activation parameters were analysed as functions of solute content and temperature. In the four alloys containing Ni, Mn, Al and Si, solid-solution softening occurs below 250 K while solid-solution hardening occurs above 250 K. In the alloys containing Co or Cr, neither softening nor hardening due to solute additions occurs at any temperature. Detailed analysis of thermal activation parameters leads one to conclude that the solid-solution softening in the above mentioned four alloys is due to a decrease in kink energy with increasing solute content, while in the latter two alloys no change in kink energy occurs. On the other hand, there exists a strong solute concentration dependence of the athermal component, suggesting that the solid-solution hardening is due to the interaction of dislocations with groups of substitutional solute atoms that create lattice and modulus misfits.

1. Introduction

It is commonly known that the alloying of solute atoms in solution often causes an increase in the deformation stress, referred to as solid-solution strengthening, while in a number of alloy systems [1–9] a decrease in strength by alloying, referred to as solid-solution softening, has been observed. In b c c metals, solid-solution softening occurs at low temperatures and hardening at high temperatures [10]. The present paper is concerned with solid-solution softening and hardening due to the alloying of 0.2 to 1 at % of Al, Co, Cr, Ni, Mn and Si to Fe, and the mechanisms for softening and hardening are discussed.

It is generally accepted that plastic deformation of metals and alloys is thermally activated and the yield or flow stresses σ are composed of the thermal component σ^* and athermal component σ_μ so that

$$\sigma = \sigma^* + \sigma_\mu \tag{1}$$

The increase in σ with decreasing temperature usually results from an increase in σ^*, while its contribution is less at high temperatures. Accordingly when σ^* decreases by alloying at low temperatures, solid-solution softening predominantly appears on σ^* [9, 11]. On the other hand the contribution of σ^* is rather small at high temperatures so that an increase in σ due to alloying can be attributed mainly to solid-solution hardening through σ_μ [11].

If the rate controlling mechanism for low temperature deformation is overcoming the Peierls barrier by nucleating double kinks, solid-solution softening would occur if the dislocation velocity is controlled by the rate of formation of double kinks [12]. Accordingly, alloying of solute atoms would probably change the thermal component for deformation and the formation energy of double kinks and their widths. All of the thermally activation parameters such as the thermal component σ^*, dislocation velocity–stress exponent m^*, activation area A^*, activation enthalpy ΔH, kink energy H_k and kink width W_k will be influenced by alloying.

The solid-solution hardening is due to the direct interaction between dislocations and solute atoms. There have been many theories [13–16] that predict various concentration dependence, linear to a power law. Kostorz [17] and Koss [18] report that the concentration dependence of the athermal component should test the theory's validity. Accordingly, the effects of alloying element and its concentration on the athermal component σ_μ are studied here in detail.

2. Experimental procedures

2.1. Materials and specimen preparation

Eighteen binary iron-base alloys containing 0.2, 0.5 and 1 at % solutes of Co, Cr, Al, Si, Ni and Mn, respectively, were prepared in an induction furnace by melting each element of high purity with electrolytic iron. Prior to alloying, electrolytic iron was scavenged of its interstitial carbon from the iron matrix by adding an equivalent amount of Ti [19] in vacuum of less than 10^{-3} torr. The chemical analyses of 18 binary alloys are given in Table I. The alloyed ingots were first homogenized at 1543 K for 10.8 ks, and were hot-rolled to 30 mm in thickness after heating at 1473 K for 1.8 ks. Then, they were cold-rolled to a final thickness of 0.8 mm.

0022–2461 © *1996 Chapman & Hall*

TABLE I Chemical analyses (at %) of six binary iron alloys

Alloys	C	Si	Mn	P	S	N	O	Ti
0.19 Cr	0.019	0.010	0.011	0.007	0.005	0.007	0.010	0.034
0.47 Cr	0.023	0.008	0.010	0.007	0.004	0.008	0.010	0.041
0.94 Cr	0.019	0.010	0.011	0.007	0.004	0.007	0.011	0.066
0.24 Co	0.019	0.010	0.009	0.009	0.005	0.012	0.012	0.043
0.54 Co	0.023	0.010	0.012	0.009	0.003	0.009	0.009	0.041
1.00 Co	0.014	0.010	0.009	0.007	0.003	0.010	0.009	0.076
0.21 Ni	0.023	0.010	0.010	0.007	0.005	0.008	0.011	0.041
0.52 Ni	0.019	0.008	0.008	0.007	0.003	0.007	0.012	0.031
1.03 Ni	0.019	0.010	0.009	0.007	0.003	0.008	0.010	0.054
0.20 Mn	0.019	0.010	0.20	0.009	0.005	0.076	0.001	0.033
0.51 Mn	0.014	0.012	0.51	0.007	0.005	0.072	0.002	0.035
1.01 Mn	0.014	0.012	1.01	0.009	0.007	0.088	0.001	0.050
0.11 Al	0.019	0.010	0.010	0.007	0.005	0.009	0.010	0.106
0.48 Al	0.019	0.014	0.008	0.007	0.004	0.006	0.003	0.070
0.98 Al	0.023	0.016	0.008	0.007	0.004	0.007	0.004	0.070
0.20 Si	0.019	0.020	0.009	0.007	0.005	0.010	0.014	0.033
0.51 Si	0.014	0.050	0.010	0.007	0.003	0.010	0.017	0.054
0.99 Si	0.014	0.099	0.010	0.007	0.005	0.008	0.013	0.050

The tensile specimens were machined to obtain a gauge length of 25 mm with a cross-section of $2 \times 0.8\ \mathrm{mm}^2$. To eliminate the grain size effect on strength, all of the tensile specimens were annealed in a vacuum of approximately 10^{-6} torr at various temperatures (953 to 1073 K) for a predetermined period of time (1.8 to 18 ks) to have an average grain size of 20 μm. The grain size was measured under an optical microscope using the conventional linear intercept method.

2.2. Simple tensile and relaxation tests

Simple tensile tests at a strain rate of $3.3 \times 10^{-4}\ \mathrm{s}^{-1}$ were conducted on a screw-driven Instron to obtain the stress–strain behaviours in the temperature range of 77 to 450 K. Several baths (liquid nitrogen at 77 K, gasoline chilled with liquid N_2 at 160 K, dry ice–acetone at 195 K, ethanol chilled with liquid N_2 at 225 and 250 K, ice and water at 274 K, water at 297 K, and silicon oil (KF54) heated to 325 to 450 K) were used to obtain constant temperatures during tests. All the bath temperatures were controlled within ± 2 K.

Stress–relaxation tests were conducted at several temperatures; a specimen was first deformed in tension at a predetermined plastic strain at a strain rate of $3.3 \times 10^{-4}\ \mathrm{s}^{-1}$, and the crosshead was stopped to allow the load to relax for 60 s. These operations were repeated at plastic strains of approximately 1, 2, 4, 8 and 16%, respectively. The load relaxation was recorded on a linear recorder at a chart speed of $8.3\ \mathrm{mm\,s}^{-1}$ using a zero suppression multiplier. The specimen exhibiting the Luders elongation was stress-relaxed only in the plastic flow region.

3. Results

3.1. Temperature dependence of the yield and flow stresses

The values of true stress and true plastic strain for six binary alloys of three compositions each were calculated as a function of temperature. As typical examples, Fig. 1 shows the true stress–strain behaviour for Fe–1.03 at % Ni and Fe–1.00 at % Co alloys deformed at a strain rate of $3.3 \times 10^{-4}\ \mathrm{s}^{-1}$ and 77 to 450 K. Both the yield and flow stresses at a given strain increased with decreasing temperature in all alloys, suggesting that a thermally activated process is responsible for the plastic deformation. A sharp yield drop and extended Luders elongation are characteristic to the stress–strain behaviour at 77 K, but this tendency is reduced with increasing deformation temperature, and above 250 K only smooth, parabolic behaviour is observed, regardless of the alloy species and compositions.

The stress at the proportional limit is plotted against temperature for Fe–Ni and Fe–Co alloys, as examples, as a function of their composition in Fig. 2. The behaviour for the Fe–Ni alloys is representative of those for the Fe–Al, Fe–Mn and Fe–Si alloys (alloys in the first category), while that for the Fe–Co is representative of that for the Fe–Cr alloys (alloys in the second category). In the latter alloy systems, the temperature dependence of the proportional-limit stress (defined as the yield stress here) is exactly the same as that for a Fe–0.05 at % Ti alloy which simulates an interstitial-free iron [19]. In other words, neither solid-solution softening nor hardening are observed in these two alloys regardless of their composition. On the other hand, the former four alloys exhibit solid-solution softening below 250 K and solid-solution hardening above 250 K. Fig. 3 is presented for the temperature dependence of the yield stress in the former four alloys containing about 1 at % of the respective solute element in order to compare each other with that for an interstitial free iron. Again, solid-solution softening below 250 K and solid-solution hardening above 250 K are clearly seen. The contribution of alloying elements to solid-solution softening and hardening will be discussed later in terms of the thermal and athermal components of the flow stress.

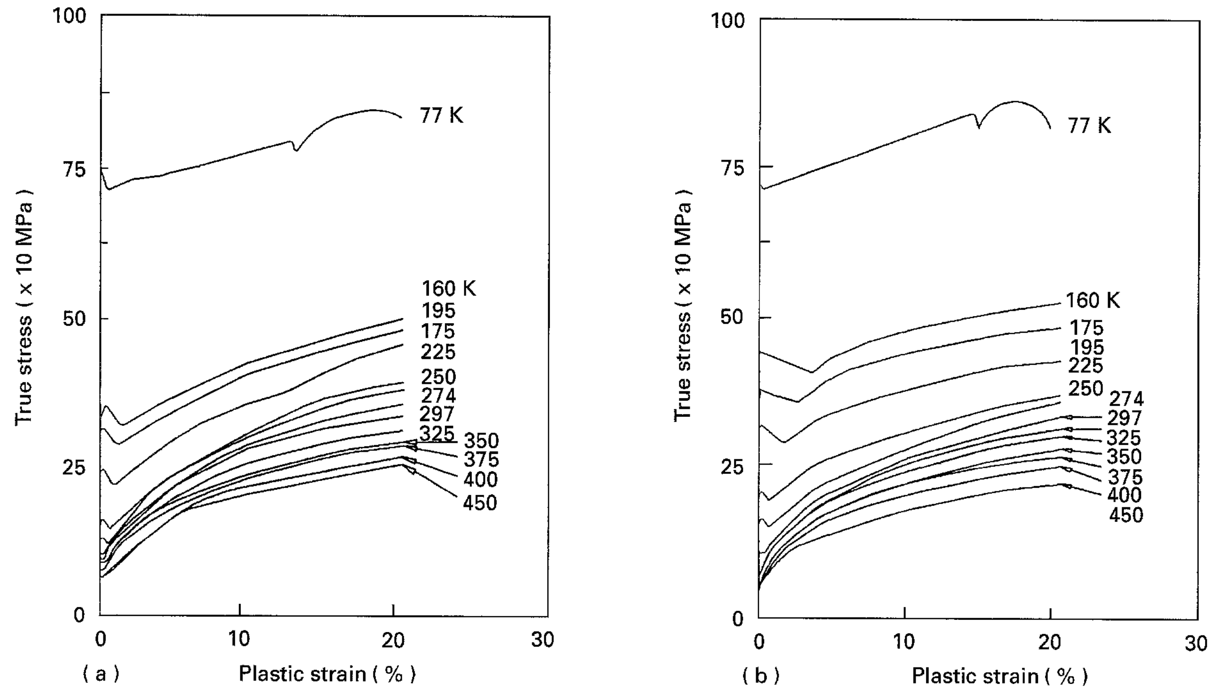

Figure 1 Stress–strain behaviour at various temperatures for (a) Fe–1.03 at % Ni and (b) Fe–1.00 at % Co alloys to represent the first and second category alloys, respectively.

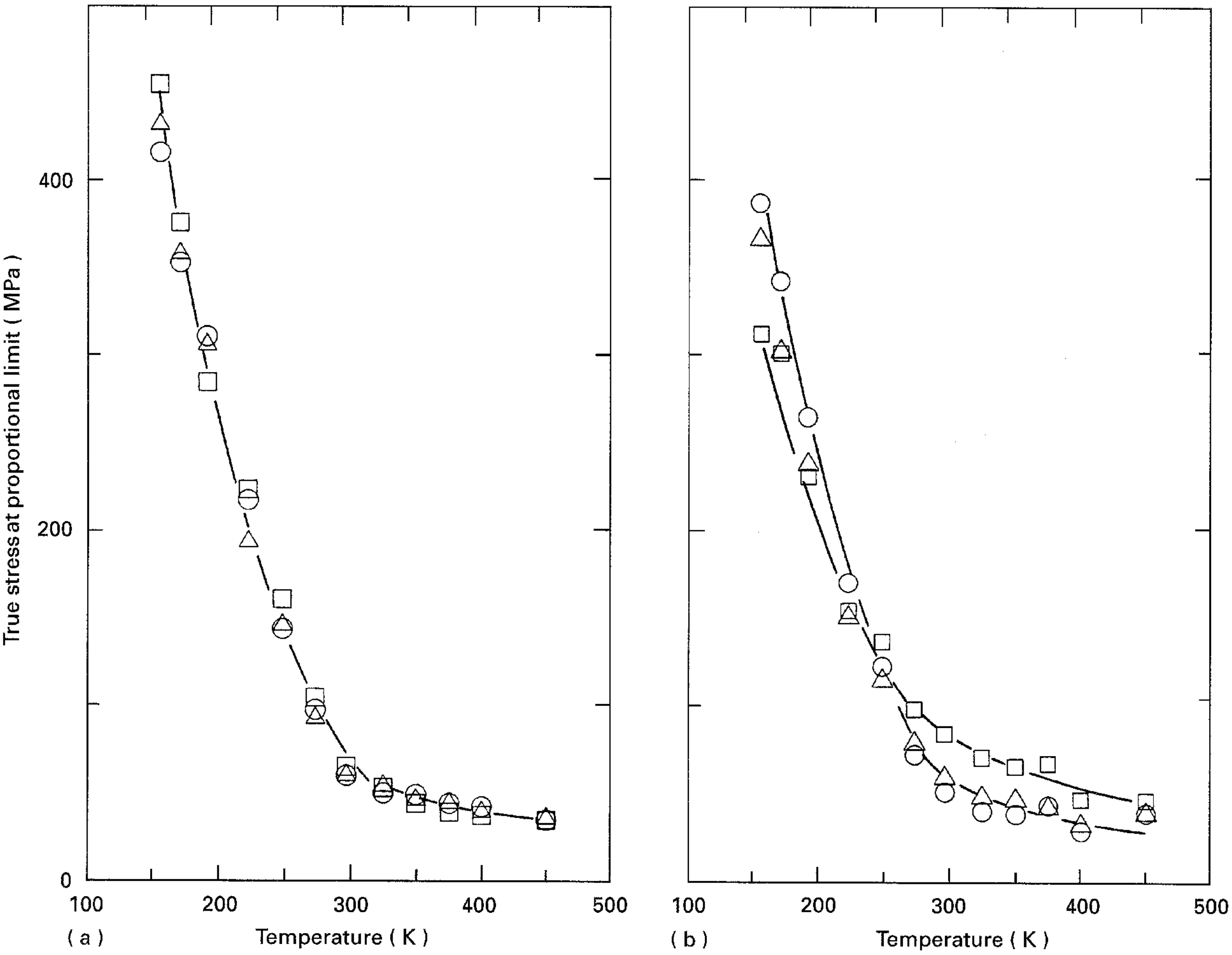

Figure 2 Temperature dependence of the stress at proportional limit for (a) Fe–Ni and (b) Fe–Co alloys as a function of solute concentration. (a) Key: ○ pure iron, ○ Fe–0.21 at % Ni; △ Fe–0.52 at %Ni, □ Fe–1.03 at % Ni. (b) Key: ○ pure iron, ○ Fe–0.24 at % Co, △ Fe–0.54 at % Co, □ Fe–1.00 at % Co.

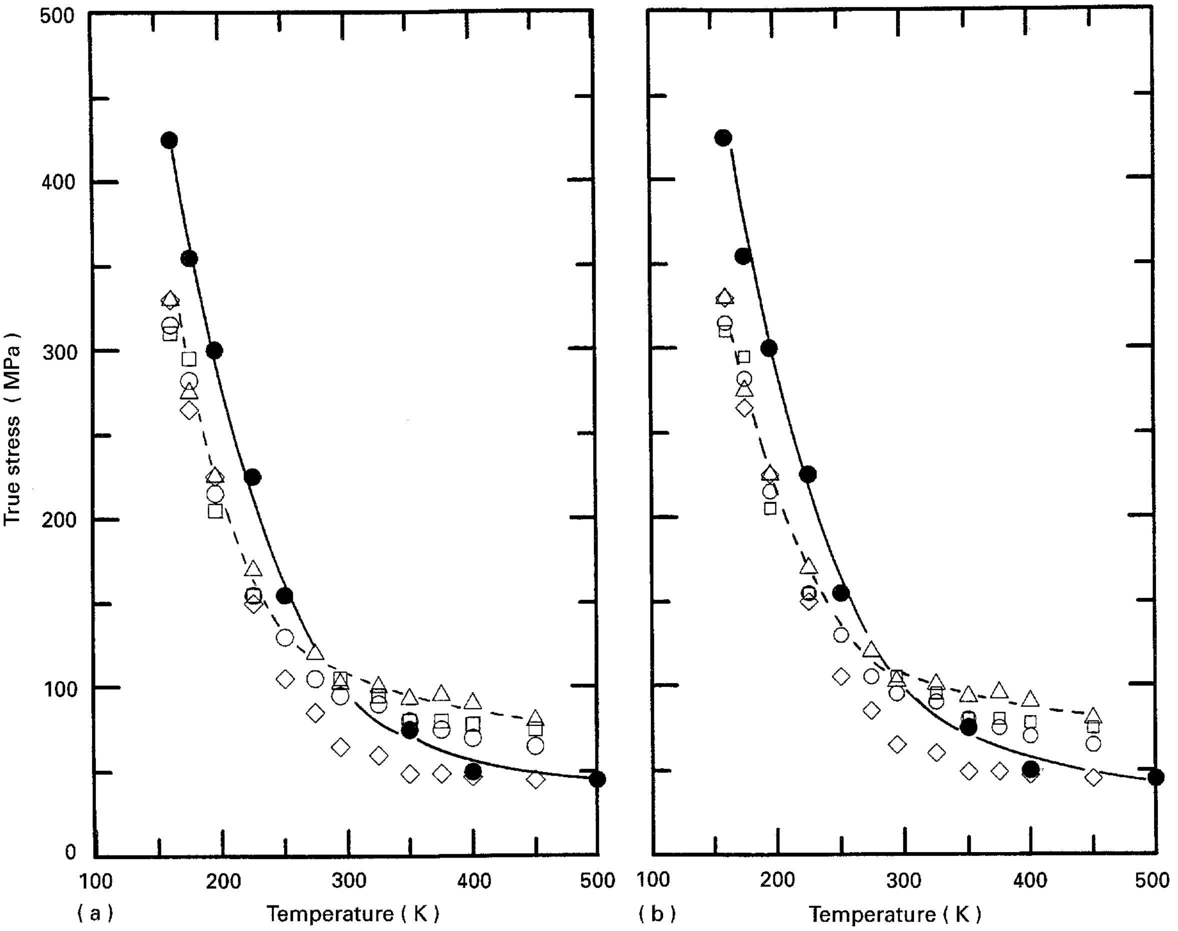

Figure 3 Temperature dependence of the (a) yield stress and (b) lower yield stress for a comparison of various alloys containing approximately 1 at % solute atoms. Key: ● pure iron, ○ Fe–1.03 at % Ni, △ Fe–0.99 at % Si, □ Fe–1.01 at % Mn, ◇ Fe–0.98 at % Al.

3.2. Thermal and athermal components of the stress

The athermal component, $\sigma_{\mu T}$ of the flow stress σ at any temperature T can be calculated by using the Seeger extrapolation method [20] as

$$\sigma_{\mu T} = (\mu_T/\mu_{T_0})\,\sigma_{\mu T_0} \qquad (2)$$

where μ_T and μ_{T_0} are the shear moduli at temperatures T and T_0 and $\sigma_{\mu T_0}$ is the athermal stress at T_0. The thermal component, σ^* can then be obtained by subtracting σ_μ from the flow stress σ. The values of the thermal component thus calculated are given in Table II for the 18 alloys as a function of temperature.

The temperature dependence of the thermal component is depicted Fig. 4 typically for Fe–Ni and Fe–Co alloys as a function of their composition. It is clearly seen in this figure that the thermal component decreases with increasing deformation temperature and increasing solute content in the first category alloys, while in the second category alloys the concentration dependence is not observed regardless of temperature. Fig. 4 is reproduced from Fig. 3 to clearly demonstrate the solute dependence of the thermal component as a function of temperature. Fig. 5 shows the solute dependence of the thermal component at 160 and 195 K where the solid-solution softening is exhibited by the first category alloys and the degree of softening is higher in the order of Si, Al, Mn and Ni, while Co and Cr do not contribute to the softening at all.

3.3. Activation parameters

The imposed strain rate, $\dot{\varepsilon}_t$ during a constant strain rate test can be divided into two components, elastic $\dot{\varepsilon}_e$ and plastic $\dot{\varepsilon}_p$

$$\dot{\varepsilon}_t = \dot{\varepsilon}_e + \dot{\varepsilon}_p \qquad (3)$$

When the crosshead is stopped for the load to relax, $\dot{\varepsilon}_t = 0$ and

$$\dot{\varepsilon}_p = -\,\dot{\varepsilon}_e = -\,K_m\dot{\sigma} \qquad (4)$$

where $K_m = 1/E + A_0/Sl_0$, and A_0 and l_0 are the gauge area and length of a specimen, respectively, at the beginning of relaxation, $\dot{\sigma}$ is the stress rate, and S and E the spring constant and Young's modulus, respectively. The plastic strain rate is also related to the velocity of mobile dislocations through the Orowan equation [21]

$$\dot{\varepsilon}_p = \alpha\rho_m \mathbf{b} v \qquad (5)$$

where α is a geometric factor, ρ_m is the density of mobile dislocations, v is their average velocity and $\mathbf{b}$ is the Burgers vector. It is presently assumed that a functional relationship between the average velocity of dislocations and the effective stress σ^* acting on dislocations can be described by a Johnston–Gilman type equation [22]

$$v = B(\sigma^*)^{m^*} \qquad (6)$$

TABLE II Averaged values of the thermal component, σ^* ($\times 10$ MPa) at various temperatures

	Temperature (K)						
Alloy	160	175	195	225	250	274	297
0.19 Cr	27.1	23.1	17.8	10.7	6.6	3.8	2.0
0.47 Cr	27.4	22.7	17.8	10.5	7.1	3.2	2.0
0.94 Cr	27.6	22.5	17.0	11.1	7.0	3.8	1.8
0.24 Co	27.2	22.8	17.3	11.3	6.8	3.6	1.5
0.54 Co	27.8	23.4	16.5	11.5	7.2	3.4	1.6
1.00 Co	27.4	22.1	16.7	11.0	6.2	3.2	1.3
0.21 Ni	24.2	21.4	16.3	9.3	4.5	2.3	1.2
0.52 Ni	22.0	18.8	12.4	7.0	3.8	1.7	1.1
1.03 Ni	18.2	15.3	10.4	4.9	2.6	1.3	1.0
0.20 Mn	24.5	22.2	16.1	9.0	4.8	2.8	0.4
0.51 Mn	21.8	19.3	12.5	7.1	3.5	2.0	0.7
1.01 Mn	17.7	15.1	9.4	4.7	2.5	1.5	1.0
0.11 Al	22.6	19.5	14.5	9.4	4.6	2.2	0.4
0.48 Al	20.9	18.5	12.8	6.7	3.0	1.9	0.5
0.98 Al	17.2	14.8	9.9	4.6	2.4	1.4	0.9
0.20 Si	23.0	21.8	15.2	8.2	4.7	2.7	1.0
0.51 Si	19.6	16.8	10.4	5.3	3.3	1.6	1.1
0.99 Si	14.0	10.9	8.0	3.5	1.6	0.9	0.7

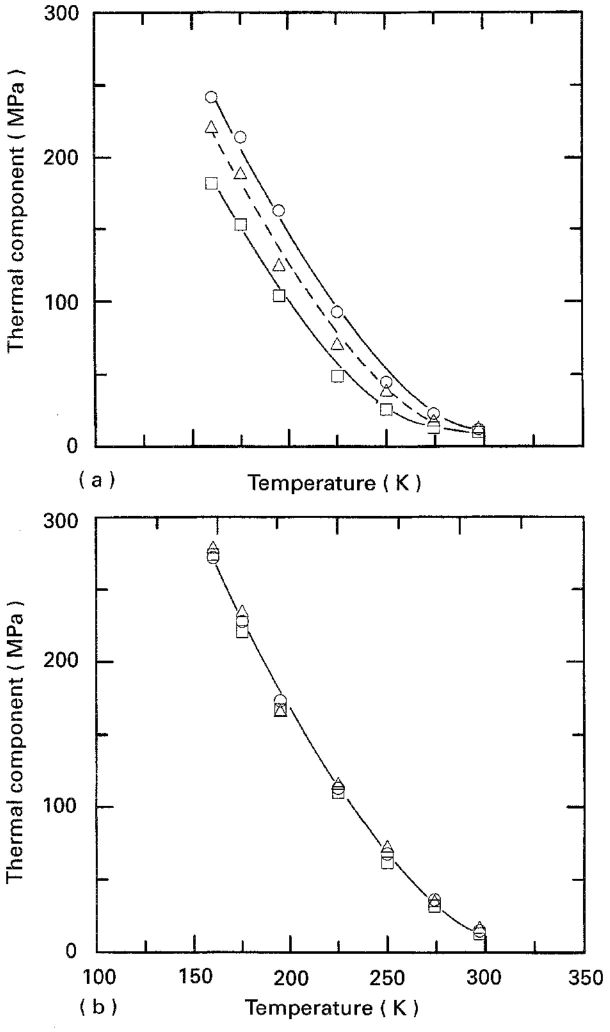

Figure 4 Temperature dependence of the thermal component of the flow stress for (a) Fe–Ni and (b) Fe–Co alloys as a function of solute content (a) Key: ○ Fe–0.21 at % Ni, △ Fe–0.52 at % Ni, □ Fe–1.03 at % Ni. (b) Key: ○ Fe–0.24 at % Co, △ Fe–0.54 at % Co, □ Fe–1.00 at % Co.

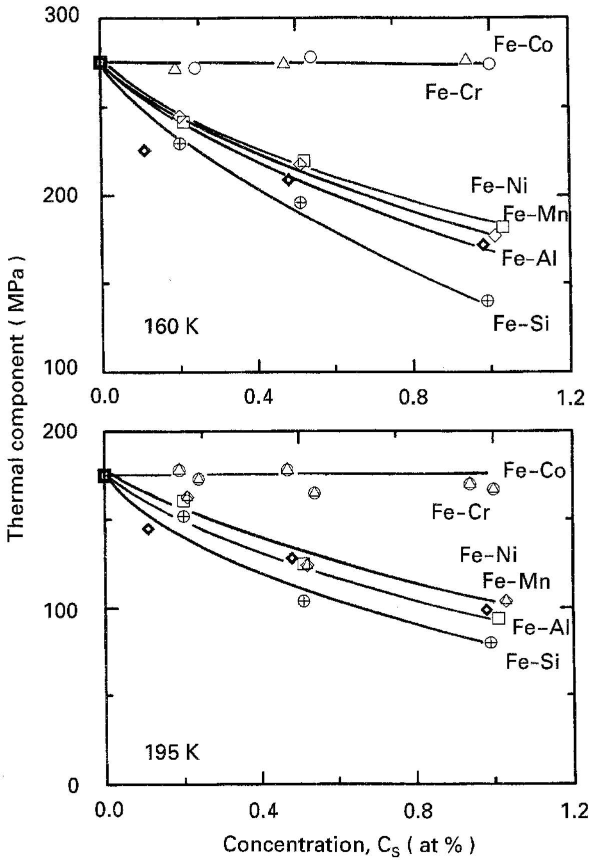

Figure 5 Concentration dependence of the thermal component for binary iron alloys at 160 and 195 K.

where B and m^* are constant, both being dependent on temperature. Equations 4 to 6 are combined to yield

$$-\dot{\sigma} = (\alpha \mathbf{b} B/K_{\mathrm{m}})\rho_{\mathrm{m}}(\sigma^*)^{m^*} \tag{7}$$

where the effective stress is the imposed stress σ_0 minus its athermal component σ_μ. Integration of Equation 7 under the assumption of constant ρ_{m}, m^* and σ_μ with respect to the relaxation time t yields

$$\sigma^* = \sigma_0 - \sigma_\mu = K(t + a)^{-n} \tag{8}$$

where $n = 1/(m^* - 1)$, $K = [\alpha \mathbf{b} B \rho_{\mathrm{m}}(m^* - 1)/K_{\mathrm{m}}]^{-n}$ and a is an integration constant. Further, differentiation of Equation 8 with respect to t yields

$$\dot{\sigma}^* = -nK(t + a)^{-n-1} \tag{9}$$

where $\dot{\sigma}^*$ becomes equal to be σ under the condition of constant σ_μ. Then, the dislocation velocity–stress exponent m^* can be calculated from the slope of the negative stress rate versus relaxation time, i.e.

$$m^* = Q/(Q + 1) \tag{10}$$

where Q is the slope of the log–log plot at long time periods, $t \gg a$ [23].

An analysis of the stress relaxation data yields the activation area, A^* defined by the equation

$$A^* = (MkT/\mathbf{b})[\Delta \ln v/\Delta\sigma^*] \tag{11}$$

where M, k and T are the Taylor factor ($M = 2.75$ is used in the present analysis), Boltzmann constant and temperature, respectively. A combination of Equations 4, 5 and 11 yields

$$A^*(t) = (MkT/\mathbf{b})[\Delta \ln(-\dot{\sigma})/\Delta\sigma^* - \Delta \ln \rho_m/\Delta\sigma^*]. \qquad (12)$$

3.4. Activation area, A^*

Using Equation 12, the values of activation area at plastic strains of 1, 2, 4, 8 and 16% were calculated. Okazaki *et al.* [24] have shown that both the mobile dislocation density and the athermal component remain constant only for the first short period of relaxation. Accordingly the activation area here was calculated by using only the early portion of the relaxation curve.

The strain dependence of activation area is illustrated in Fig. 6 for Fe–Ni alloys at 225 K as a typical example. The activation area does not depend on the plastic strain so that it can be averaged over the plastic region. The averaged values of activation area for all the alloys at various temperatures are tabulated in Table III, and it is seen that the activation area significantly increases with increasing temperature but slightly increases with increasing solute content, and this trend in terms of the activation area versus solute content as a function of temperature is illustrated for Fe–Ni alloys in Fig. 7 as a typical example. Also illustrated in Fig. 8 is the contribution of different solute elements to the activation area at 297 and 195 K, where it is clearly seen that the contribution is greater in the order of Mn, Ni, Al and Si, while Co and Cr do not alter the activation area at all regardless of their content.

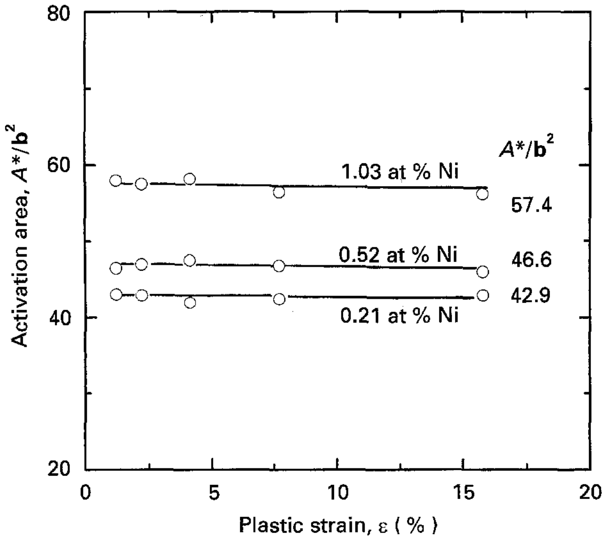

Figure 6 Strain dependence of the activation area for Fe–Ni alloy at 225 K as a function of solute content.

TABLE III Averaged values of activation area, $A^*/\mathbf{b}^2$ in six binary iron alloys at various temperatures

	Temperature (K)						
Alloy	160	175	195	225	250	274	297
0.19 Cr	24.7	25.6	28.6	36.1	47.1	57.3	94.5
0.47 Cr	25.1	25.6	28.5	38.7	46.3	58.1	94.5
0.94 Cr	25.6	25.8	28.9	36.2	47.7	57.4	94.5
0.24 Co	24.3	25.4	31.0	36.5	47.2	58.6	94.9
0.54 Co	25.4	27.2	33.6	37.0	45.8	54.6	94.5
1.00 Co	25.3	26.2	30.1	36.8	48.7	58.5	95.5
0.21 Ni	26.0	27.0	29.5	42.9	52.5	84.0	116.6
0.56 Ni	26.5	27.5	30.2	46.6	58.4	92.1	129.6
1.03 Ni	27.0	27.8	33.0	57.5	67.0	102.7	148.5
0.20 Mn	25.7	26.2	29.5	45.1	59.4	99.8	123.9
0.51 Mn	26.2	27.0	30.6	49.4	73.7	106.8	134.5
1.01 Mn	27.0	27.8	36.2	64.5	86.2	116.1	148.5
0.11 Al	26.4	26.0	28.3	42.0	53.0	84.5	110.3
0.48 Al	26.2	26.3	29.6	46.4	57.4	92.6	125.7
0.98 Al	26.8	27.2	33.6	55.1	67.1	98.9	136.8
0.20 Si	24.1	27.7	29.6	43.5	52.4	82.3	108.8
0.51 Si	25.3	28.8	30.3	46.3	57.4	89.4	116.6
0.99 Si	28.8	28.9	34.2	54.5	64.0	90.3	127.6

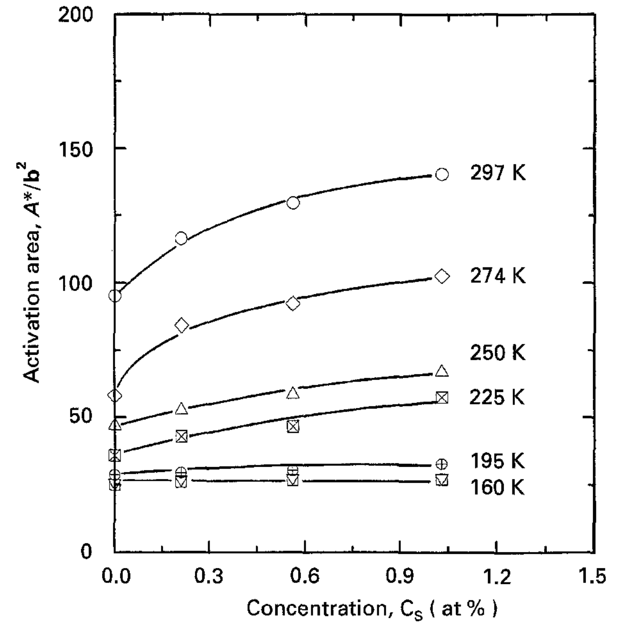

Figure 7 Concentration dependence of the activation area for Fe–Ni alloys as a function of temperature.

3.5. Dislocation velocity–stress exponent, m^*

The dislocation velocity–stress exponent, m^* that has been obtained from Equation 6 has also been described by Christian [25] in the form of

$$m^* = A^*\mathbf{b}\sigma^*/MkT \qquad (13)$$

where A^* is the activation area, $\mathbf{b}$ is the Burgers vector, σ^* is the effective stress, M is the Taylor factor (2.75 is used here), k is the Boltzmann constant and T is absolute temperature. The values of m^* calculated by using the above equation and the values of A^* and σ^* at T are tabulated in Table IV for the 18 alloys.

Depicted in Fig. 9 is the dislocation velocity–stress exponent m^* versus solute content as a function of temperature for Fe–Si and Fe–Co alloys, given here as typical examples. The former alloys exhibit the trend that m^* decreases with increasing solute content

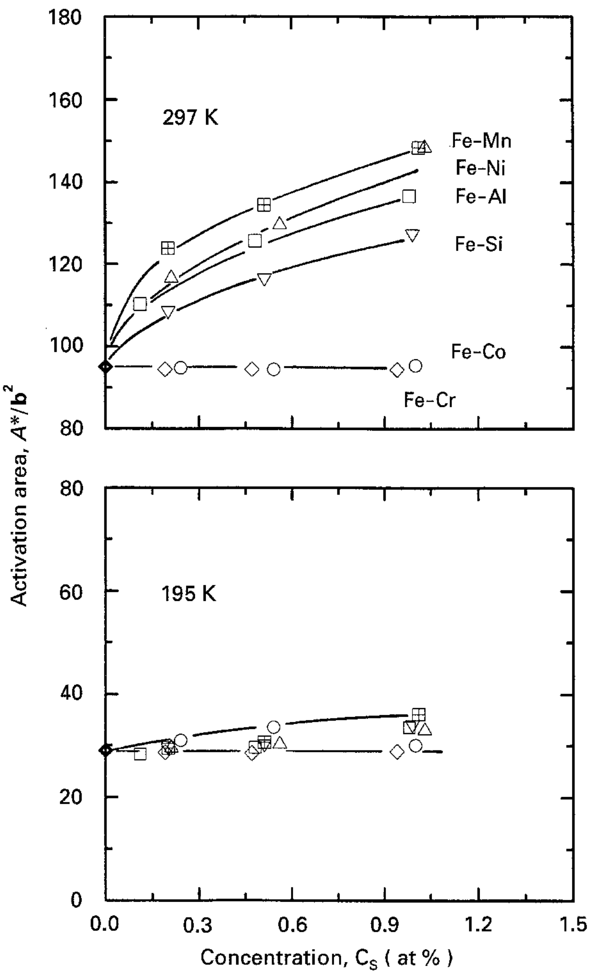

Figure 8 A comparison of the concentration dependence of the activation area for various alloys at 195 and 297 K.

TABLE IV Averaged values of dislocation velocity–stress exponent, m^* in six binary iron alloys at various temperatures

Alloy	Temperature (K) 160	175	195	225	250	274	297
0.19 Cr	17.1	13.8	10.6	7.0	5.1	3.2	2.6
0.47 Cr	17.5	13.5	10.6	7.4	5.4	2.8	2.6
0.94 Cr	18.0	13.5	10.3	7.3	5.4	3.2	2.3
0.24 Co	16.8	13.5	11.2	7.5	5.2	3.1	2.0
0.54 Co	18.2	14.8	11.6	7.7	5.4	2.8	2.1
1.00 Co	17.7	13.5	10.5	7.3	4.9	2.8	1.7
0.21 Ni	16.0	13.5	10.1	7.2	3.9	2.9	1.9
0.52 Ni	14.9	12.0	7.8	5.9	3.6	2.3	2.1
1.03 Ni	12.5	9.9	7.2	5.1	2.8	2.0	1.9
0.20 Mn	16.0	13.6	9.9	7.4	4.6	4.2	0.7
0.51 Mn	14.6	12.1	8.0	6.4	4.2	3.2	1.3
1.01 Mn	12.2	9.8	7.1	5.5	3.5	2.4	2.0
0.11 Al	15.2	11.8	8.6	7.2	4.0	2.8	0.6
0.48 Al	14.0	11.3	7.9	5.6	2.8	2.6	0.9
0.98 Al	11.7	9.4	7.0	4.6	2.6	2.1	1.7
0.20 Si	14.1	12.7	9.4	6.5	4.0	3.3	1.5
0.51 Si	12.6	11.3	6.3	4.4	3.1	2.1	1.8
0.99 Si	10.3	7.3	5.7	3.5	1.7	1.2	1.2

and increases with decreasing temperature, this trend being similarly observed in the alloys of the first category. On the other hand, the Fe–Co alloys belonging to the second category exhibit a strong dependence of m^* on temperature but not on the solute content. This trend is also seen in the Fe–Cr alloys of the second category. The m^* values in both Fe–Co and Fe–Cr alloys are almost the same as those in an interstitial-free iron. Fig. 10 shows the temperature dependence of m^* for six alloys containing different solute atoms of approximately 1 at %, the values of m^* decreasing in the order of Ni, Mn, Al and Si at all the temperatures studied. A similar trend has already been seen for σ^*.

3.6. Activation energy, ΔH

Conrad [26] and Wiedersich and Conrad [27, 28] has shown that the activation energy ΔH can be described by

$$\Delta H = -kT^2(\Delta \ln\dot{\varepsilon}/\Delta\sigma^*)_T(\Delta\sigma^*/\Delta T)_{\dot{\varepsilon}} \quad (14)$$

where $\dot{\varepsilon}$ is the strain rate. By introducing A^* into the above equation, one obtains

$$\Delta H = -(1/M)TA^*\mathbf{b}(\Delta\sigma^*/\Delta T)_{\dot{\varepsilon}} \quad (15)$$

where $(\Delta\sigma^*/\Delta T)_{\varepsilon}$ can be obtained from the slope of σ^* versus T curve for each alloy. The calculated values of ΔH at various temperatures and ΔH_0 at T_0 are tabulated in Table V for the 18 alloys. As typical examples, the dependence of the activation energy, ΔH on temperature T are shown in Fig. 11 for Fe–Ni and Fe–Co alloys, where it is seen that ΔH linearly increases with increasing temperature in the alloys of both categories. The first category alloys exhibit the solute concentration dependence of ΔH while the second category alloys do not. Fig. 12 shows the dependence of activation energy on the thermal component, $\tau^*(\tau^* = \sigma^*/M)$ for Fe–Ni and Fe–Co alloys containing three different solute concentrations as typical examples. The behaviour of the Fe–Cr alloys is quite similar to that of Fe–Co alloys, exhibiting no concentration dependence.

The temperature T_0 at which the thermal component, σ^* becomes zero was determined from the temperature dependence of the yield stress, and the values of T_0 and ΔH_0 (ΔH at T_0) are also tabulated in Table V. In the second category alloys, the values of T_0 and ΔH_0 are independent of the solute content, both being the same as those for an interstitial-free iron [19]. On the other hand, in the first category alloys both ΔH_0 and T_0 decrease with increasing solute content, but the T_0 values are not significantly different from each other. Fig. 13 shows the dependence of ΔH on the effective shear stress, τ^* for six alloys containing approximately 1 at % of the respective solute atoms. This figure makes a comparison of the contribution from different elements to the values of ΔH at a constant τ^*, the contribution being in the order of Co and Cr, Ni, Mn, Al and Si. It should be noted that this order is similar to those seen for other activation parameters such as A^*, m^* and σ^*.

3.7. Athermal component, σ_μ

It is normally conceived that the athermal component of the flow stress, σ_μ depends on the strain ε, grain size d, solute content C_s and the deformation temperature

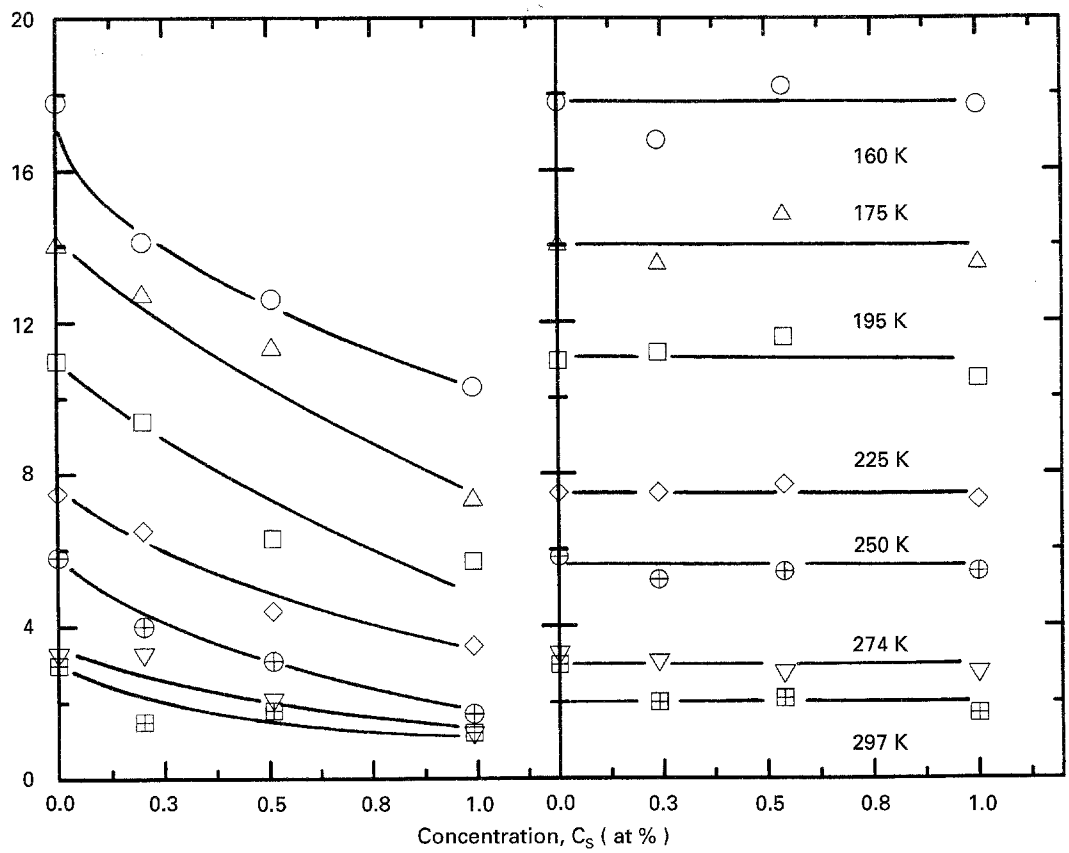

Figure 9 Concentration dependence of the dislocation velocity–stress exponent, m^* for (a) Fe–Si and (b) Fe–Co alloys as a function of temperature. Key: ○ 160 K; △ 175 K; □ 195 K; ◇ 225 K; ○ 250 K; ▽ 274 K; ○ 297 K.

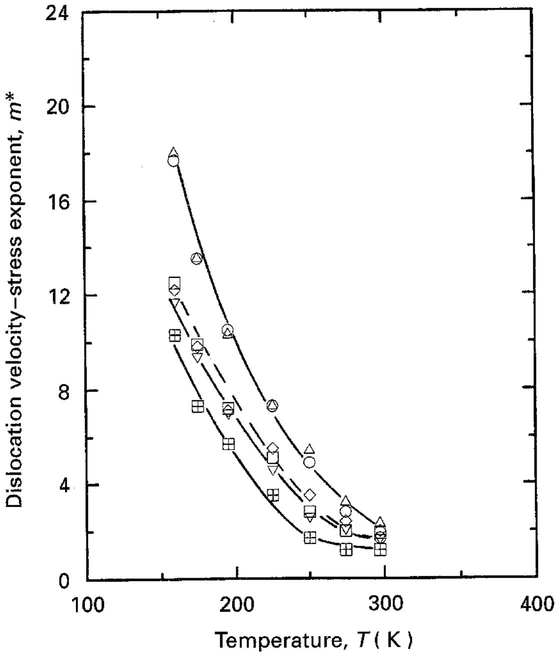

Figure 10 Temperature dependence of the dislocation velocity–stress exponent, m^* for a comparison of various alloys containing approximately 1 at % solute. Key: ○ Fe–1.00 at % Co; △ Fe–0.94 at % Co, □ Fe–1.03 at % Ni; ◇ Fe–1.01 at % Mn; ▽ Fe–0.98 at % Al; ○ Fe–0.99 at % Si.

T only through its shear modulus;

$$\sigma_\mu = f(\varepsilon, d, C_s, T). \qquad (16)$$

In this experiment, d was kept constant at approximately 20 μm. To eliminate the strain dependence, the strain was extrapolated to 0 so that the athermal component could be compared with respect to the solute content.

Labusch [29, 30] has presented a model of solid-solution strengthening modified from the previous Fleischer–Friedel [31–33] and Mott–Nabarro [34, 35] models. It has the $C_s^{2/3}$ dependence. Accordingly in Fig. 14 the athermal component at 297 K is plotted against $C_s^{2/3}$ for six alloy systems, indicating that a linear relationship exists within experimental errors in all alloys. Of significance is that the slope of the straight line through the respective data points increases in the order of Mn, Ni, Al and Si for the first category alloys but the second category alloys with Co or Cr do not exhibit the concentration dependence at all. Although the data only at 297 K are shown here, this $C_s^{2/3}$ dependence can be observed at all temperatures below T_0 in the first category alloy systems.

4. Discussion

4.1. Rate controlling mechanism of plastic deformation

Friedel [36] derived the temperature dependence of σ^*, by considering the thermal activation required to overcome the Peierls–Nabarro barrier by double kink formation, as

$$\sigma^* = \sigma_0^*(1 - T/T_0)^2 \qquad (17)$$

where σ_0^* is the Peierls stress at 0 K. The thermal component σ^* in Fe–Co alloys is plotted in Fig. 15 against $(1 - T/T_0)$ as a function of the Co content,

TABLE V Values of activation energy, ΔH (eV) at various temperatures, H_0 and T_0 in six binary iron alloys

Alloy	Temperature (K) 160	175	195	225	250	274	297	ΔH_0 (eV)	T_0 (K)
0.19 Cr	0.35	0.38	0.40	0.48	0.54	0.60	0.63	0.73	335
0.47 Cr	0.35	0.38	0.40	0.51	0.53	0.62	0.63	0.73	335
0.94 Cr	0.36	0.38	0.41	0.48	0.54	0.62	0.63	0.73	335
0.24 Co	0.34	0.37	0.44	0.48	0.54	0.62	0.63	0.73	335
0.54 Co	0.36	0.40	0.47	0.49	0.53	0.58	0.64	0.73	335
1.00 Co	0.36	0.39	0.42	0.49	0.56	0.62	0.64	0.73	335
0.21 Ni	0.33	0.36	0.40	0.50	0.54	0.59	0.66	0.71	330
0.54 Ni	0.31	0.33	0.39	0.47	0.50	0.57	0.60	0.67	325
1.03 Ni	0.30	0.32	0.38	0.45	0.46	0.53	0.57	0.63	320
0.20 Mn	0.31	0.35	0.40	0.49	0.51	0.57	0.63	0.69	330
0.51 Mn	0.30	0.34	0.39	0.46	0.51	0.55	0.62	0.66	325
1.01 Mn	0.30	0.34	0.39	0.45	0.48	0.55	0.61	0.62	320
0.11 Al	0.32	0.35	0.40	0.49	0.55	0.60	0.62	0.70	330
0.48 Al	0.29	0.32	0.40	0.47	0.49	0.57	0.58	0.66	325
0.98 Al	0.28	0.30	0.36	0.43	0.46	0.51	0.56	0.61	320
0.20 Si	0.31	0.35	0.38	0.47	0.50	0.54	0.61	0.67	330
0.51 Si	0.31	0.35	0.37	0.47	0.49	0.51	0.60	0.64	325
0.99 Si	0.30	0.33	0.37	0.42	0.44	0.47	0.52	0.57	320

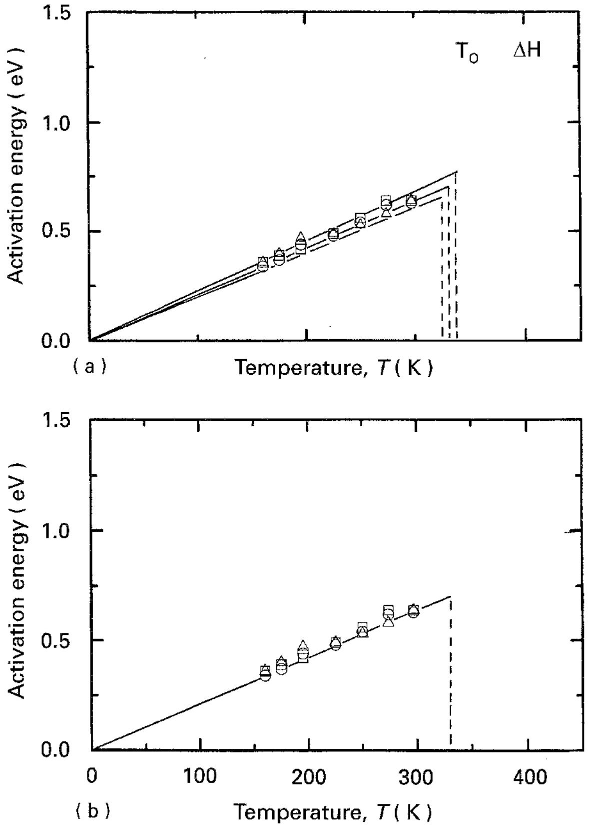

Figure 11 Temperature dependence of the activation energy ΔH for (a) Fe–Ni alloys, ○ 0.21 % at. % Ni 330 K 0.71 e.v.; △ 0.52 at. % Ni 325 K 0.67 ev; □ 1.03 at. % Ni 320 K 0.63 ev; and (b) Fe–Co alloys, ○ 0.24 at. % Co 335 K 0.73 ev; △ 0.52 at. % Co 335 k 0.73 ev; □ 1.00 at. % Co 335 K 0.73 ev, as a function of solute concentration.

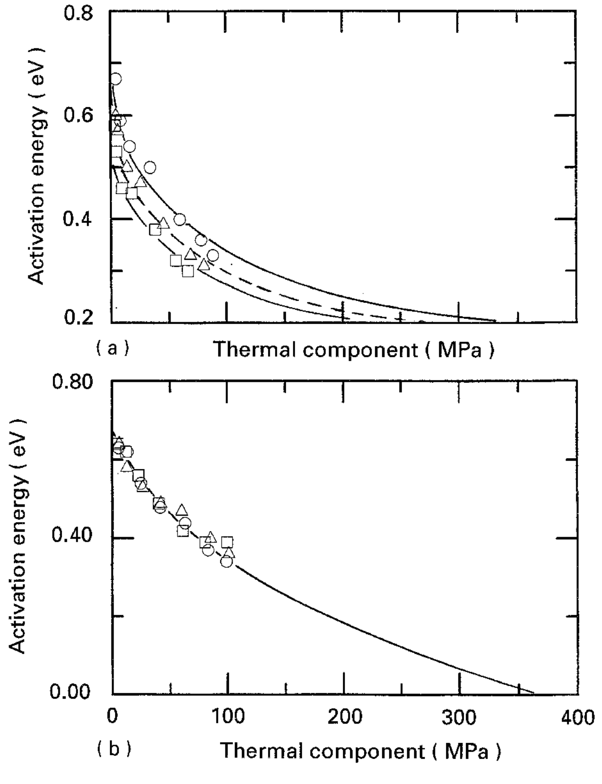

Figure 12 Dependence of the activation energy on the thermal component for (a) Fe–Ni and (b) Fe–Co alloys as a function of solute concentration. (a) Key: ○ Fe–0.21 at % Ni, △ Fe–0.52 at % Ni; □ Fe–1.03 at % Ni. (b) Key: ○ Fe–0.24 at % Co; △ Fe–0.54 at % Co; □ Fe–1.00 at % Co.

indicating that a linear relationship exists through the data points regardless of the Co content. A similar behaviour is also observed in the Fe–Cr alloys. Both alloys in the second category exhibit no concentration dependence. On the other hand, the first category alloys exhibit a significant concentration dependence such that the slope of the straight line decreases with increasing solute content; in other words σ_0^* decreases with increasing solute content. In order to clearly show this concentration dependence on σ_0^*, it is plotted in Fig. 16 against C_s for all alloys. It is seen that neither Co nor Cr exhibit the concentration dependence, but the first category alloys exhibit the strong decreasing dependence with increasing solute content in the order of Ni, Mn, Al and Si.

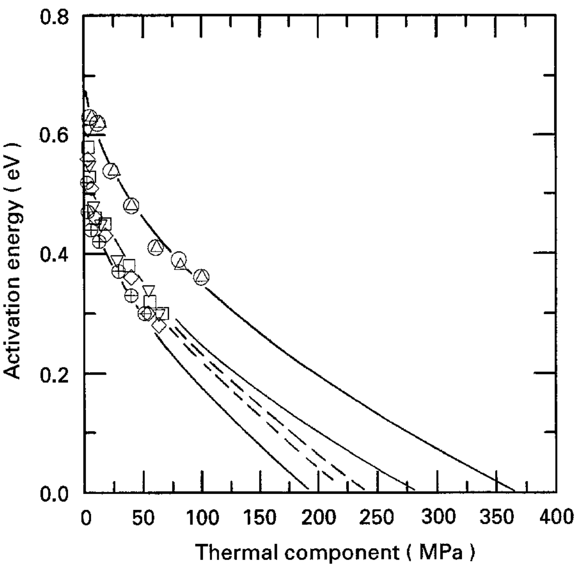

Figure 13 The activation energy versus the thermal component for a comparison of various alloys containing approximately 1 at % solute. Key: ○ Fe–1.00 at % Co; ◇ Fe–0.94 at % Cr; ○ Fe–1.03 at % Ni; □ Fe–1.01 at % Mn; △ Fe–0.98 at % Al; ◇ Fe–0.99 at % Si.

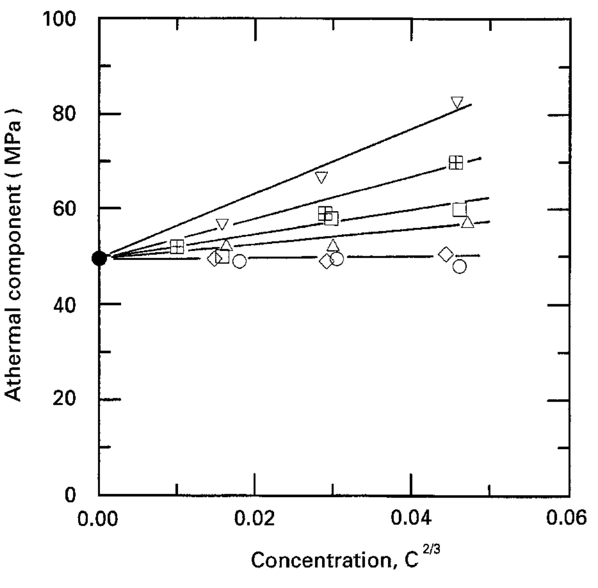

Figure 14 Concentration dependence of the athermal component at 297 K for various alloys. Key: ▽ Fe–Si; ⊞ Fe–Al; □ Fe–Ni; △ Fe–Mn; ◇ Fe–Co; ○ Fe–Cr.

Alternatively Dorn and Rajnak [37] showed a temperature dependence of σ^* in the form of (T/T_0) (μ_T/μ_{T_0}) versus (σ^*/σ_0^*) . The present data points roughly fit the theoretical curve with $\alpha = -1$ in all alloy systems. The present data satisfy the theories both by Friedel and by Dorn and Rajnak and conclude that the rate controlling mechanism in the low temperature deformation of these dilute binary alloys is the overcoming of the Peierls barrier by nucleating double kinks in dislocations with the aid of thermal fluctuation.

4.2. Kink energy and its width

Dorn and Rajnak [37] described the kink energy H_k and width W_k in the forms of

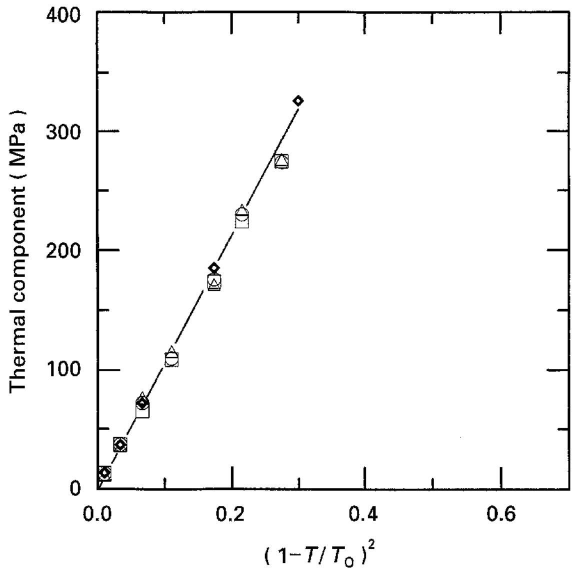

Figure 15 Temperature dependence of the thermal component for Fe–Co alloys as a function of solute concentration. Key: ○ pure iron; ○ Fe–0.24 at % Co; △ Fe–0.54 at % Co ($\sigma_0^* = 101.9$); □ Fe–1.00 at % Co. ◇ Fe.

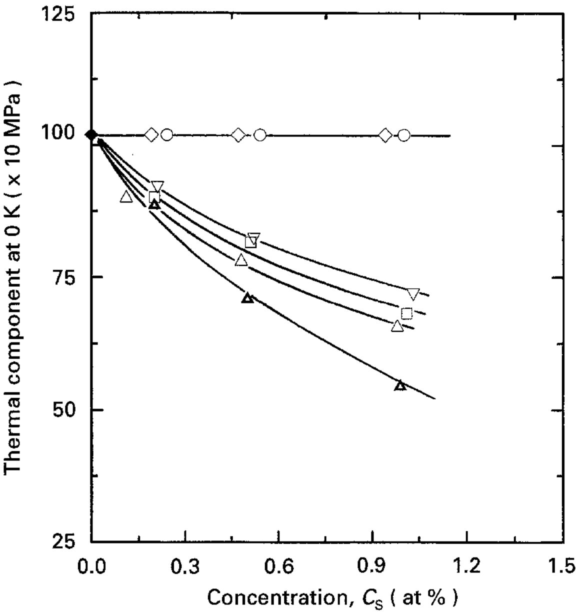

Figure 16 Concentration dependence of the thermal component at 0 K for various alloys. Key: ◆ pure iron; ○ Fe–Co; ◇ Fe–Cr; ▽ Fe–Ni; □ Fe–Mn; △ Fe–Si; ▲ Fe–Al.

$$\Delta H_0/2H_k = (T/T_0)(\mu_{T_0}/\mu_T) \tag{18}$$

and

$$W_k = (\pi/2)(2aE_0/\mathbf{b}\tau_0^*)^{1/2} \tag{19}$$

where a is the distance between close-packed rows of atoms, E_0 is the line energy of a dislocation ($= \mu\mathbf{b}^2$, μ is the shear modulus) and τ_0^* is the thermal component of the shear stress ($\tau^* = \sigma^*/M$) at 0 K. Equation 18 indicates that the activation energy ΔH_0 at T_0 becomes equal to twice the kink energy H_k so that it can be calculated from the activation energy ΔH_0 already listed in Table V.

The values of H_k thus obtained are plotted in Fig. 17 against the solute content, C_s for six alloy

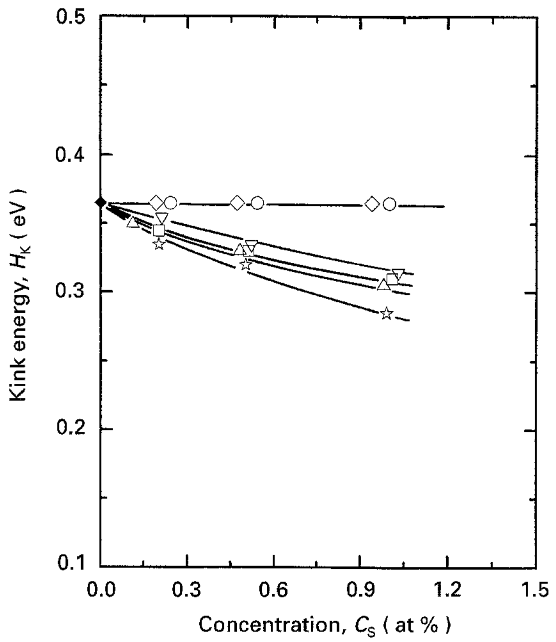

Figure 17 Concentration dependence of the kink energy for various alloys. Key: ◆ pure iron; ○ Fe–Co; ◇ Fe–Cr; ○ Fe–Ni; □ Fe–Mn; △ Fe–Al; ☆ Fe–Si.

systems. Although Co and Cr do not influence the kink energy, the second category elements decrease the kink energy with increasing solute content in the order of Ni, Mn, Al and Si. On the other hand, the kink width W_k increases with increasing solute content in the order of Ni, Mn, Al and Si as shown in Fig. 18, where it is again seen that Co and Cr have no contribution to the kink width. From Figs 17 and 18 it can be concluded that in the first category alloys an increase in the solute content leads to an increase in the kink width and a decrease in the kink energy. These changes eventually result in a decrease in the effective stress, leading to solid-solution softening.

4.3. Solid-solution softening

So far several models have been proposed to the solid-solution softening in b c c metals; (1) removal of interstitial atoms by solute atoms [38–41], (2) an increase in the mobile dislocation density [42, 43], (3) promotion of cross-slip by solute atoms [44, 45] and (4) a decrease in the lattice friction stress or creation of local distortions that help overcome the lattice friction stress [2, 4, 46, 47]. The scavenging effect of substitutional elements was considered for solid-solution softening in Fe–Cr [41], Fe–V [5] and Ta–Re [5] alloys. Jolley [45] observed the occurrence of cross slips even at 50 K and attributed the ease of cross-slipping to the softening. Tanaka and Watanabe [48] regarded the solid-solution softening as due to a change in the formation energy of double kinks. Sato and Meshii [10] presented a mechanism such that kink nucleation on screw dislocations can be facilitated by localized strain centres at low temperatures to produce the softening. Urakami and Fine [49] provided evidence that screw dislocations after deformation are helical by being bent by clustered solute atoms.

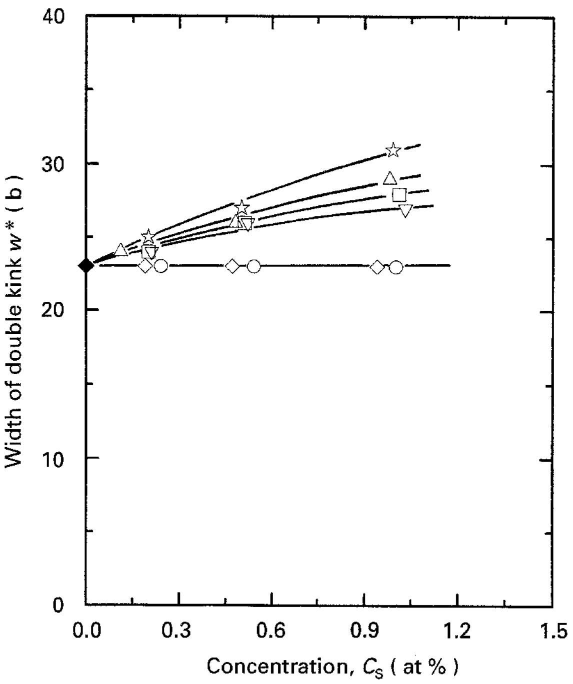

Figure 18 Concentration dependence of the kink width for various alloys. Key: ◆ pure iron; ○ Fe–Co; ◇ Fe–Cr; ▽ Fe–Ni; □ Fe–Mn; △ Fe–Al; ☆ Fe–Si.

The absence of solid-solution softening in the Fe–Co and Fe–Cr is attributed to negligibly small atomic misfits produced by Co and Cr, as indicated by the lattice parameters [50]. Accordingly both the kink energy and its width were independent of the solute content, indifferent from those in interstitial-free iron. On the other hand, the solid-solution softening due to the first category elements is attributed to larger atom size misfits, as indicated by the lattice parameter measurements [50, 51]. Both the kink energy decrease and kink width increase with increasing solute content, that are experimentally observed, are due to the enhanced kink nucleation through a strong solute atom–dislocation interaction, eventually resulting in a decrease in the effective stress σ^* with increasing solute content.

4.4. Solid solution hardening

When the obstacle to dislocation motion is mainly an individual solute atom, Fleischer and Friedel [31–33] proposed the following relation between the effective stress τ_0^* at 0 K and the solute content C_s of the form

$$\tau_0^* \mathbf{b} = f_0^{*3/2} C_s^{1/2} \mathbf{b}^{-1} (2E_L)^{-1/2} \qquad (20)$$

where f_0^* is a maximum force of the interaction between an individual solute atom and a dislocation and E_L is the dislocation line tension. When the obstacle is a group of solute atoms, Mott and Nabarro [34, 35] proposed the following relation,

$$\tau_0^* \mathbf{b} = f_0^{*4/3} C_s^{2/3} \mathbf{b}^{-4/3} (4E_L)^{-1/3} w^{1/3} D \qquad (21)$$

where w is the width of the individual solute obstacle ($w = \mathbf{b}$) and D is a constant of the order of 1/3.

Whether the strengthening in a given alloy is due to the Fleischer–Friedel model (Equation 20) or the Mott–Nabarro model (Equation 21) depends on the magnitudes of f_0^* and C_s. Labusch [15], based on the degree of dislocation bow-out, discriminates between these two models; the Fleischer–Friedel model prevails if

$$(2f_0^* \mathbf{b}^2/144\, C_s E_L)^{1/2} > w \qquad (22)$$

but the Mott–Nabarro model does if

$$(f_0^* \mathbf{b}^2/4\, C_s E_L)^{1/2} > w \qquad (23)$$

The adoption of the present data to the left-hand sides of Equation 22 or 23 indicates that Equation 23 can be better satisfied since the left-hand side of Equation 23 is in the range of 3.9 to 24.5 **b** while that of Equation 22 is in the range of 0.52 to 2.5 **b**. These values naturally decrease with increasing solute concentration. It is therefore concluded that the present data satisfy the condition for the Mott–Nabarro model, i.e. the strengthening is due to the interaction of a dislocation with a group of solute atoms. It is noted that the Mott–Nabarro model indicates the concentration dependence of the athermal component is a 2/3 power (Equation 21), and the present data have already verified this concentration dependence in Fig. 14.

The solid-solution hardening theories currently available consider the atomic size misfit parameter, $\varepsilon_a(= (1/a)(\mathrm{d}a/\mathrm{d}C)$, where a is the lattice parameter), the modulus misfit parameter, ε'_G ($= \varepsilon_G/(1 + |\varepsilon_G/2|)$, $\varepsilon_G = (1/G)/\mathrm{d}G/\mathrm{d}C$), where G is the shear modulus) or combination of these misfits. However, only the theory that has a 2/3 power dependence on the solute concentration is due to Labusch [15], while the others have linear or 1/2 power dependence. According to Labusch, an increase in the athermal component stress due to the solute can be described by

$$\sigma_\mu = 2G(|\varepsilon'_G| + \alpha|\varepsilon_a|)^{4/3}\, C_s^{2/3} \qquad (24)$$

where α is a constant of 2. Using the values of ε'_G and ε_a reported by Takeuchi [51] and Speich *et al.* [50], the present data on σ_μ are plotted against $(|\varepsilon'_G| + 2|\varepsilon_a|)^{4/3}\, C_s^{2/3}$ in Fig. 19 for six alloys. It is possible to draw a straight line through the data points for the respective alloy, and it is seen that the first category alloys containing Si, Al, Mn and Ni have a 2/3 power concentration dependence while the second category alloys containing Co and Cr have no concentration dependence. Therefore it is concluded that the solid-solution strengthening by the first category elements is due to the combined effect of size misfit and modulus misfit.

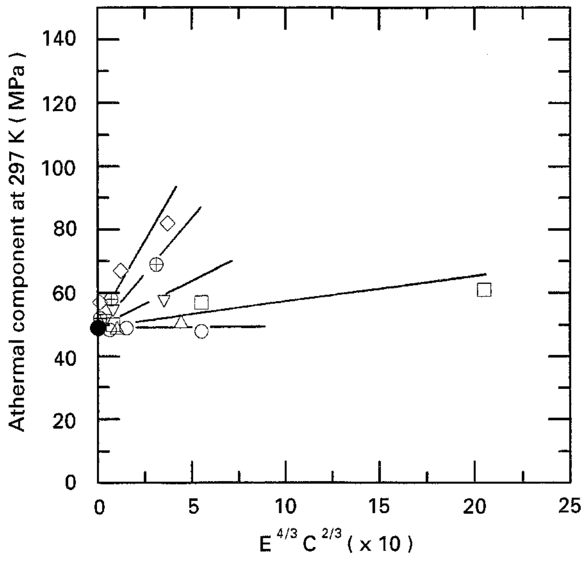

Figure 19 A combined effect of the solute concentration and lattice and modulus misfits on the athermal component ($I = 297$ K). Key: ◇ Fe–Si; ⊕ Fe–Al; ▽ Fe–Mn; □ Fe–Ni; △ Fe–Co; ○ Fe–Cr.

References

1. G. C. DAD and R. J. ARSENAULT, *Scripta Metall.* **2** (1968) 495.
2. R. J. ARSENAULT *Acta Metall.* **17** (1969) 1291.
3. S. TAKEUCHI, Y. YOSHIDA and T. TAOKA, *Trans JIM* **9** (1968) 715.
4. R. S. RAWLINGS and W. A. NEWEY, *Mater Sci. Eng.* **4** (1969) 271.
5. R. L. SMIALEK, G. L. WEBB and T. E. MITCHELL, *Scripta Metall.* **4** (1970) 33.
6. K. V. RAVI and R. GIBALA, *Acta Metall.* **18** (1970) 623.
7. S. K. LAHIRI and M. E. FINE, *Met. Trans.* **1** (1970) 1495.
8. B. C. PETERS and A. A. HENDRICKSON, *ibid.* **1** (1970) 2271.
9. W. A. SPITZIG and W. C. LESLIE, *Acta Metall.* **19** (1971) 1143.
10. A. SATO and M. MESHII, *ibid.* **21** (1973) 753.
11. S. SAKUI, K. SATO and T. SAKAI, *J. Iron Steel Inst., Jpn.* **58** (1972) 47.
12. H. SUZUKI, "Rate Processes in Plastic Deformation of Materials" (American Society for Metals, Reeding, MA 1975) p. 47.
13. R. L. FLEISCHER, *Acta Metall.* **11** (1963) 203.
14. J. C. M. LI "Dislocation Dynamics" (McGraw–Hill, New York, 1968) p. 87.
15. R. LABUSCH, *Phys. Status Solidi* **41** (1970) 659.
16. S. TAKEUCHI, *J. Phys. Soc. Jpn.* **27** (1969) 929.
17. G. KOSTORZ, *Z. Metallkd.* **59** (1968) 941.
18. D. A. KOSS, *Met. Trans.* **2** (1971) 245.
19. K. OKAZAKI, M. KAGAWA and Y. AONO, *Z. Metallkd.* **67** (1976) 47.
20. A. SEEGER, *Z. Naturforsch.* **9a** (1954) 758, 819, 856.
21. E. OROWAN, *Proc. Phys. Soc.* **52** (1940) 8.
22. W. G. JOHNSTON and J. J. GILMAN, *J. Appl. Phys.* **30** (1959) 129.
23. J. C. M. LI, *Can. J. Phys.* **45** (1967) 493.
24. K. OKAZAKI, Y. AONO and M. KAGAWA, *Acta Metall.* **24** (1976) 1121.
25. J. W. CHRISTIAN, *ibid.* **15** (1967) 1257.
26. H. CONRAD and H. WIEDERSICH, *ibid.* **8** (1960) 128.
27. H. CONRAD, *J. Metals* **16** (1964) 582.
28. *Idem, Mater. Sci. Eng.* **6** (1970) 265.
29. R. LABUSCH, *Phys. Status Solidi* **41** (1970) 659.
30. R. LABUSCH, *Acta Metall.* **20** (1965) 917.
31. R. L. FLEISCHER and W. R. HIBBARD, in NPL Conference on the Relation between Structure and Mechanical Properties, Vol. 1 (HMSO, London, 1963) p. 262.
32. R. L. FLEISCHER, "The Strengthening of Metals", edited by D. Peckner (Reinhold Pub. Corp., N.Y., 1964) p. 93.
33. J. FRIEDEL, "Electron Microscopy and Strength of Crystals", edited by G. Thomas and J. Washburn (Interscience, N.Y., 1963) p. 605.
34. F. R. N. NABARRO, *Proc. Soc.* **58** (1964) 669.
35. N. F. MOTT and F. R. N. NABARRO, Rep. Conf. on Strength of Solids (London Phys. Soc., 1948) 1.
36. J. FRIEDEL, "Dislocations" (Addison-Wesley, Reeding, Mass., 1964) p. 1052.
37. J. E. DORN and S. RAJNAK, *Trans. AIME* **230** (1964) 1052.
38. R. D. RAWLINGS and C. W. A. NEWEY, *Mater. Sci. Eng.* **4** (1969) 271.

39. R. L. SMIALEK, G. L. WEBB and T. E. MITCHELL, *Scripta Metall.* **4** (1970) 33.
40. K. V. RAVI and R. GIBALA, *Acta Metall.* **18** (1970) 623.
41. C. E. LACY and M. GENSAMER, *Trans. ASM* **32** (1944) 88.
42. Y. NAKADA and A. S. KEH, *Acta Metall.* **16** (1968) 903.
43. B. W. CHRIST, R. P. GUMBLE and G. V. SMITH, *Scripta Metall.* **3** (1969) 521.
44. W. JOLLEY, *Trans AIME* **242** (1968) 307.
45. *Idem, ibid.* **242** (1968) 306.
46. T. E. MITCHELL and R. L. ROFFO, *Can. Phys.* **45** (1967) 1.
47. R. J. ARSENAULT, *Acta Metall.* **15** (1967) 501.
48. T. TANAKA and S. WATANABE, *ibid.* **19** (1971) 991.
49. A. URAKAMI and M. E. FINE, *Scripta Metall.* **4** (1970) 667.
50. G. R. SPEICH, A. J. SCHWOEBLE and W. C. LESLIE, *Met. Trans.* **3** (1972) 2031.
51. S. TAKEUCHI, *J. Phys. Soc., Jpn.* **27** (1969) 929.

Received 22 December 1993
and accepted 16 August 1995